

Research Article

[MG49-LiClO₄]:[TiO₂-SiO₂] Polymer Electrolytes: In Situ Preparation and Characterization

Oon Lee Kang,¹ Azizan Ahmad,¹ Nur Hasyareeda Hassan,¹ and Usman Ali Rana²

¹Faculty of Science and Technology, Universiti Kebangsaan Malaysia, 43600 Bangi, Selangor, Malaysia

²Sustainable Energy Technologies (SET) Center, King Saud University, P.O. Box 800, Riyadh 11421, Saudi Arabia

Correspondence should be addressed to Azizan Ahmad; azizan@ukm.my and Nur Hasyareeda Hassan; syareeda@ukm.edu.my

Received 18 March 2016; Revised 8 May 2016; Accepted 23 May 2016

Academic Editor: Subramaniam Ramesh

Copyright © 2016 Oon Lee Kang et al. This is an open access article distributed under the Creative Commons Attribution License, which permits unrestricted use, distribution, and reproduction in any medium, provided the original work is properly cited.

In the present research, [MG49-LiClO₄]:[HNO₃-THF/TiO₂-SiO₂] and [MG49-LiClO₄]:[ClHNO₂-THF/TiO₂-SiO₂] polymer electrolytes were first prepared through simple stepwise *in situ* techniques: sol-gel technique and solution-cast technique. [MG49-LiClO₄]:[HNO₃-THF/TiO₂-SiO₂] and [MG49-LiClO₄]:[ClHNO₂-THF/TiO₂-SiO₂] polymer electrolytes were then characterized through different experimental techniques. [MG49-LiClO₄]:[HNO₃-THF/TiO₂-SiO₂] and [MG49-LiClO₄]:[ClHNO₂-THF/TiO₂-SiO₂] polymer electrolytes had exhibited significant structural changes upon different salt concentrations. In the present investigation, [MG49-LiClO₄]:[HNO₃-THF/TiO₂-SiO₂] and [MG49-LiClO₄]:[ClHNO₂-THF/TiO₂-SiO₂] polymer electrolytes had attained maximum ionic conductivities ($\sigma \sim 10^{-7}$ S/cm at ambient temperature; 10^{-4} S/cm at 100°C) upon 25 wt.% salt insertion. [MG49-LiClO₄]:[HNO₃-THF/TiO₂-SiO₂] and [MG49-LiClO₄]:[ClHNO₂-THF/TiO₂-SiO₂] polymer electrolytes had exhibited distinct conduction mechanisms in similar experimental configuration. [MG49-LiClO₄]:[HNO₃-THF/TiO₂-SiO₂] and [MG49-LiClO₄]:[ClHNO₂-THF/TiO₂-SiO₂] polymer electrolytes had exhibited different stability characteristics over certain operational condition.

1. Introduction

Nanocomposite polymer electrolytes are major breakthrough in solid-state electrochemical technologies [1]. PEO-LiClO₄- α -alumina polymer electrolytes were first developed in the early 1980s; recent empirical studies have focused attention on solid-state electrochemical behavior [2, 3].

Nanocomposite polymer electrolytes have shown tremendous potential in solid-state electrochemical applications. Nanocomposite polymer electrolytes are critical component in solid-state electrochemical systems [4]. Nanocomposite polymer electrolytes can serve important function as ionic conduction medium. Nanocomposite polymer electrolytes can serve another function as mechanical support barrier.

Nanocomposite biopolymer electrolytes have attained precedence over conventional electrolytes [5]. Such predominant phenomenon is considered attributable to their characteristic properties: renewable; biodegradable; biocompatible;

derivatizable; and so forth. Modified natural rubber-lithium salt-silica nanoparticle biopolymer electrolytes are often reported in the electrochemical literature [6]. Rice starch-ionic liquid-titania nanoparticle biopolymer electrolytes are also reported in the relevant literature [7].

Nanocomposite biopolymer electrolytes are often characterized as high electrochemical performance [8]. Nanocomposite biopolymer electrolytes are custom tailored to specific electrochemical characteristics: adequate ionic conductivities; negligible electronic conduction; and insignificant activation energies. Even so, some practical limitations are still encountered in solid-state electrochemical applications [9].

Nanocomposite biopolymer electrolytes are often obtained through *ex situ* techniques (i.e., dispersion techniques). Nanocomposite biopolymer electrolytes are also derived from sol-gel techniques [10].

Nanocomposite biopolymer electrolytes are often considered as multicomponent structures. In the present case, 49% poly(methyl methacrylate) grafted natural rubber (MG49)

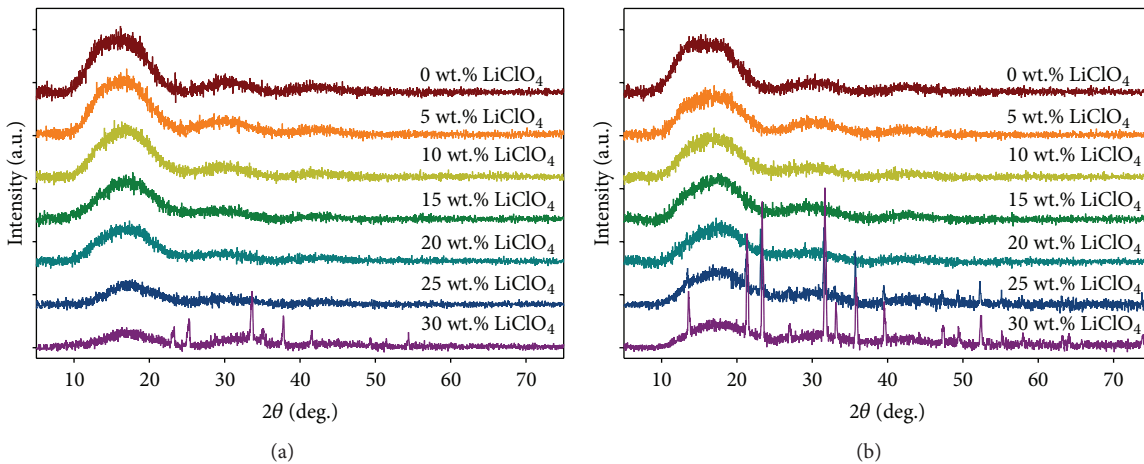


FIGURE 1: X-ray diffraction patterns: (a) [MG49- x wt.% LiClO₄]:[8.0 wt.% HNO₃-THF/TiO₂-SiO₂] and (b) [MG49- x wt.% LiClO₄]:[8.0 wt.% ClHNO₂-THF/TiO₂-SiO₂] polymer electrolytes.

is also selected as polymer host. MG49 is best regarded as superior host: excellent solvation capabilities; unique transportation properties; and superior mechanical properties [11]. Lithium perchlorate (LiClO₄) is more favorable than other lithium salts. LiClO₄ is therefore selected as dopant salt. LiClO₄ is often identified as ideal ionic salt: superior dissociative abilities; insignificant resistive characteristics; and least electronegative characteristics. Titania-silica (TiO₂-SiO₂) nanoparticles are further implemented as ceramic filler. TiO₂-SiO₂ nanoparticles have significant roles in simultaneous stabilization and performance improvement. TiO₂-SiO₂ nanoparticles are not involved in lithium transportation process.

[MG49-LiClO₄]:[HNO₃-THF/TiO₂-SiO₂] and [MG49-LiClO₄]:[ClHNO₂-THF/TiO₂-SiO₂] polymer electrolytes were first prepared through simple stepwise in situ technique: sol-gel technique and solution-cast technique. [MG49-LiClO₄]:[HNO₃-THF/TiO₂-SiO₂] and [MG49-LiClO₄]:[ClHNO₂-THF/TiO₂-SiO₂] polymer electrolytes were then characterized through different experimental techniques.

2. Experimental

2.1. Material Preparation. MG49 was purchased from Green HPSC Malaysia Sdn Bhd. LiClO₄ was purchased from Sigma-Aldrich Corporation. Metal precursors were purchased from Sigma-Aldrich Corporation. Chemical reagents were used as received unless stated otherwise.

2.2. Process Description. [MG49- x wt.% LiClO₄]:[8.0 wt.% HNO₃-THF/TiO₂-SiO₂] and [MG49- x wt.% LiClO₄]:[8.0 wt.% ClHNO₂-THF/TiO₂-SiO₂] polymer electrolytes were prepared through simple stepwise in situ technique: sol-gel technique and solution-cast technique. TiO₂-SiO₂ (70:30) sol particles were prehydrolysed in different catalyst-solvent systems: HNO₃-THF and ClHNO₂-THF systems. TiO₂-SiO₂ (70:30) sol particles were introduced into preformed MG49-LiClO₄ matrices. Resultant reaction mixtures were stirred

1/2 hours at ambient temperature. Homogeneous reaction mixtures were cast into Teflon petri dishes. Resultant thin films were dried in vacuum oven.

2.3. Polymer Electrolyte Characterization. XRD analyses were conducted on a Bruker D8 Advance diffractometer (Bruker AXS GmbH, Germany). XRD patterns were acquired in the Bragg-Brentano configuration. XRD patterns were recorded in the 2θ range (15–60°; step size 0.02°).

IR analyses were conducted on a Perkin-Elmer Spectrum 400 spectrometer (Perkin Elmer, UK). Infrared spectra were acquired in the attenuated total reflectance (ATR) mode. Infrared spectra were recorded in the mid infrared range (4000–650 cm⁻¹; spectral resolution 4 cm⁻¹).

EIS analyses were conducted on a Solartron Schlumberger SI 1286 potentiostat (Solartron Schlumberger, Farnborough, England). Impedance spectra were acquired in the alternative current (AC) modulation. Impedance spectra were recorded in the medium frequencies region (1 Hz–1 kHz).

SEM analyses were conducted on a LEO 1450 VP instrument (Carl Zeiss, Oberkochen, Germany). SEM micrographs were acquired in the backscattered electrons (BSE) mode. SEM micrographs were taken at moderate acceleration voltage (15–20 kV).

TGA analyses were conducted on a Shimadzu TGA-50 instrument (Shimadzu, Japan). TGA scans were recorded in a broad temperature range (room temperature to 600°C; scan rate 10°C min⁻¹).

DRA analyses were conducted on Anton Paar Physica MCR 501 rheometer (Anton Paar GmbH, Graz, Austria). DRA analyses were performed at isothermal condition. DRA responses were acquired in a dynamic oscillation mode.

3. Result and Discussion

3.1. Structural Characterization. X-ray diffraction patterns are shown in Figure 1. Several broad humps were observed

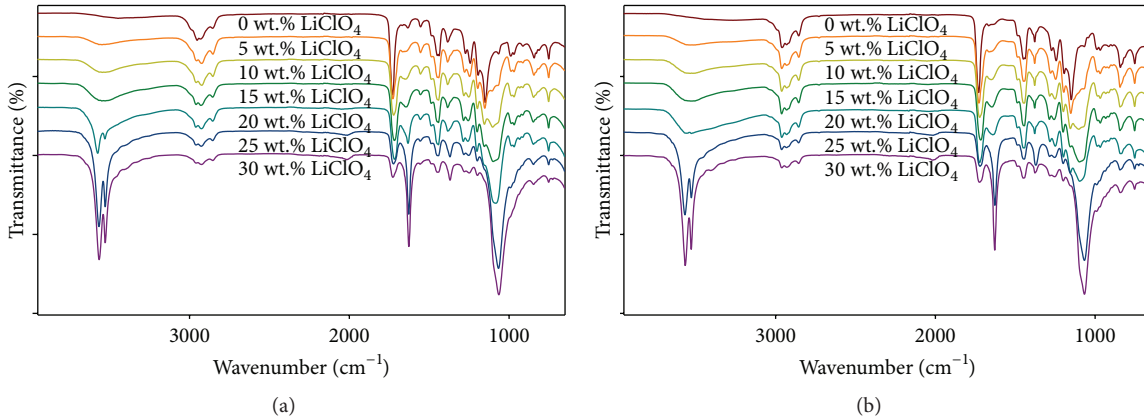


FIGURE 2: IR absorption spectra: (a) [MG49- x wt.% LiClO₄]:[8.0 wt.% HNO₃-THF/TiO₂-SiO₂] and (b) [MG49- x wt.% LiClO₄]:[8.0 wt.% CHNO₂-THF/TiO₂-SiO₂] polymer electrolytes.

at $2\theta = 15, 30, and 45° . Such broad humps are attributed to semicrystalline nature [12]. In fact, polyether side chain is still present in semicrystalline structure.$

Characteristic broad hump ($2\theta = 15^\circ$) had become flattened upon Li-salt insertion. Such predominant phenomenon is attributed to structural distortion. Characteristic broad hump is shifted upon Li-salt insertion. Characteristic broad hump is shifted to high 2-theta angle. Such predominant phenomenon is attributed to configurational alternation [13].

LiClO₄ diffraction peaks were apparent at high salt concentration (30 wt.% salt insertion). LiClO₄ diffraction peaks were observed at $2\theta = 13.5, 21.1, 23.3, 31.7, 33.1, 35.7, 39.5, 47.3, 49.3, 52.3, 58.1, and 63.1° . Such diffraction peaks are attributed to ionic association. In the literature, pure LiClO₄ diffraction peaks were observed at $2\theta = 12.1, 13.5, 21.1, 23.3, 31.7, 33.1, 35.7, 39.5, 47.3, 49.3, 52.3, 58.1, and 63.1° .$$

LiClO₄ diffraction signals are less intense in [MG49- x wt.% LiClO₄]:[8.0 wt.% HNO₃-THF/TiO₂-SiO₂] polymer electrolytes. Such preference phenomenon is attributed to strong interfacial polarization. In general, Li⁺ cation solvation is dependent on interfacial interaction [14].

IR absorption spectra are shown in Figure 2. IR absorption spectra are comparable to earlier reports. Major absorption features were detected in such vibrational regions: 3400–3600 cm⁻¹ (hydroxyl stretch); 2960–2860 cm⁻¹ (methyl stretch); 1750–1730 cm⁻¹ (carbonyl stretch); and 1250–950 cm⁻¹ (ether stretch).

Hydroxyl absorption band had become apparent upon Li-salt insertion. Hydroxyl absorption band had split into two distinct peaks (3560 and 3525 cm⁻¹). Such interference phenomenon is attributed to intramolecular hydroxyl-hydroxyl interaction. Broad shoulder band was observed at 3380 cm⁻¹. Such shoulder band is attributed to intermolecular hydroxyl-carbonyl interaction.

Carbonyl absorption band had become broadened upon Li-salt insertion. Such preference phenomenon is attributed to significant C=O-Li⁺ complexation.

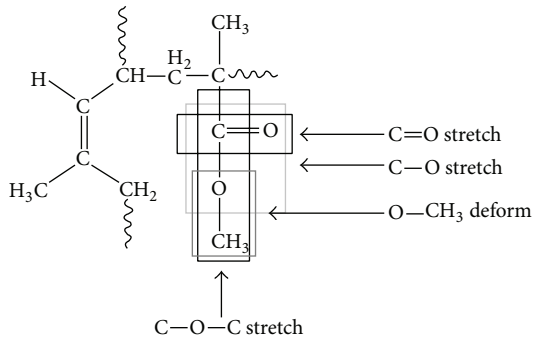


FIGURE 3: Isoprene/methyl methacrylate monomeric structure.

Ether absorption bands were observed at different vibrational modes: $\nu(\text{C}-\text{O})$, $\nu_s(\text{C}-\text{O}-\text{C})$, $\nu_{as}(\text{C}-\text{O}-\text{C})$, and $\delta(\text{O}-\text{CH}_3)$ (as shown in Figure 3). Ether absorption band is shifted upon Li-salt insertion.

LiClO₄ absorption bands were apparent at high salt concentration. LiClO₄ absorption band was observed at 1065 cm⁻¹. Such absorption bands are attributed to ionic association. In the literature, pure LiClO₄ absorption bands were observed at 1150–1080 cm⁻¹. Li⁺ absorption band was observed at 940 cm⁻¹; ClO₄⁻ absorption band was observed at 625 cm⁻¹. Surface hydroxyl absorption bands were apparent at high salt concentration. Surface hydroxyl absorption band was observed at 1630 cm⁻¹. Such hydroxyl absorption band is attributed to hygroscopic properties.

3.2. Electrochemical Characterization. Ionic conductivities were determined through electrochemical impedance technique. Ionic conductivities are correlated with Ohm's law. Ionic conductivities are regulated through multiple parameters: carrier charge, carrier concentration, and carrier mobility. Ionic conductivities are presented in Table 1. Ionic conductivities are derived from the formula:

$$\sigma = \frac{1}{R_B} \times \frac{l}{A}, \quad (1)$$

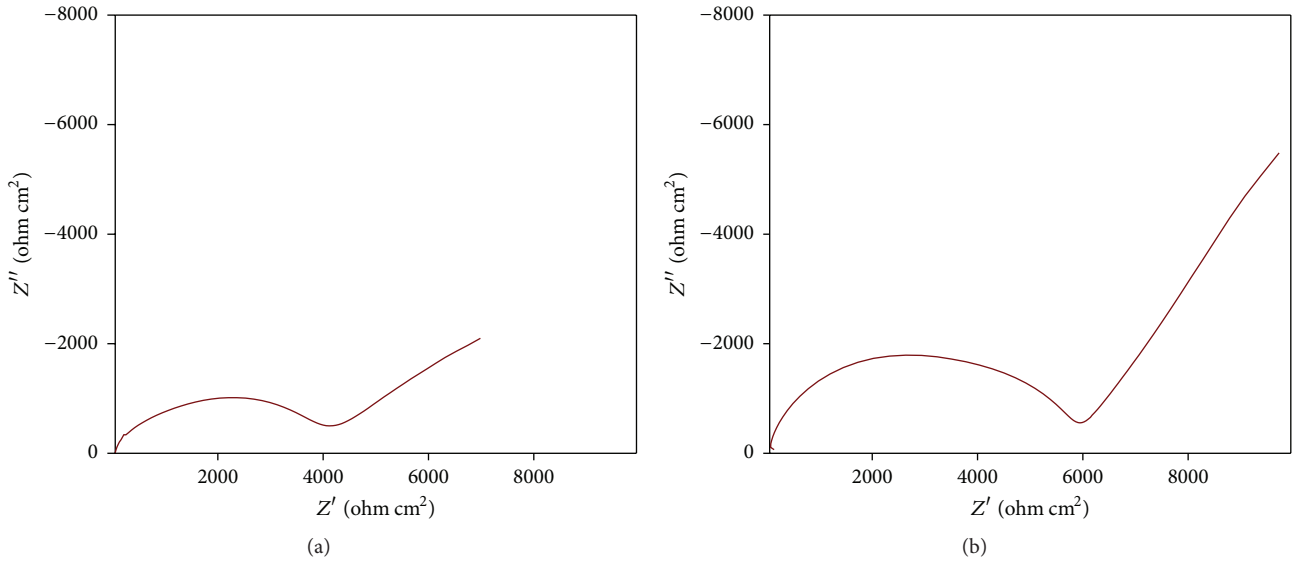


FIGURE 4: Impedance characteristic curves: (a) [MG49-25.0 wt.% LiClO₄]:[8.0 wt.% HNO₃-THF/TiO₂-SiO₂] and (b) [MG49-25.0 wt.% LiClO₄]:[8.0 wt.% ClHNO₂-THF/TiO₂-SiO₂] polymer electrolytes.

TABLE 1: LiClO₄ salt concentration-dependence ionic conductivities (S/cm) at room temperature.

LiClO ₄ (wt.%)	Ionic conductivity (S/cm)	
	[MG49- <i>x</i> wt.% LiClO ₄]:[8.0 wt.% HNO ₃ -THF/TiO ₂ -SiO ₂]	[MG49- <i>x</i> wt.% LiClO ₄]:[8.0 wt.% ClHNO ₂ -THF/TiO ₂ -SiO ₂]
0	1.19 × 10 ⁻¹¹	1.19 × 10 ⁻¹¹
5	1.63 × 10 ⁻¹¹	1.74 × 10 ⁻¹¹
10	1.35 × 10 ⁻¹⁰	2.04 × 10 ⁻¹⁰
15	4.69 × 10 ⁻⁹	1.08 × 10 ⁻⁹
20	3.09 × 10 ⁻⁷	1.60 × 10 ⁻⁸
25	5.86 × 10 ⁻⁷	4.83 × 10 ⁻⁷
30	6.01 × 10 ⁻⁹	4.24 × 10 ⁻⁹

where σ is conductivity (S·cm⁻¹); R_B is bulk resistance; l is thickness (cm); A is the cross-sectional area (cm²).

Impedance characteristic curves are shown in Figure 4. Small distorted semicircle was observed in high frequency region. Such distorted semicircle is attributed to bulk properties, that is, bulk ionic resistance and/or grain boundary resistance. Single distorted semicircle is correlated with ionic contribution dominate. Slanted spike was observed in low frequency region. Slanted spike is attributed to electrode interface properties [15].

Ionic conductivities had increased upon Li-salt insertion. Such predominant phenomenon is attributed to mobile charge carrier increment [16]. Ionic conductivities had attained maximum value at 25 wt.% salt insertion. Such preference phenomenon is ascribed to maximum C=O-Li⁺ complexation. In general, ionic transport process is mediated through strong hard-acid/hard-base interaction [17].

Ionic conductivities had decreased beyond 25 wt.% salt insertion. Such predominant phenomenon is attributed to short interionic distance. In general, ionic transport process is hindered upon ionic aggregation, that is, ionic pairs (Li⁺...ClO₄⁻) and/or ionic triplets formation. In addition, ionic transport process is hindered upon transient cross-link network formation.

In this case, however, ionic conductivities were not comparable to previous reports. Ionic conductivities are suppressed upon rotational hindrance. Such predominant phenomenon is correlated with interparticle interaction. Ionic conductivities were also high in [MG49-*x* wt.% LiBF₄]:[50 wt.% EC]:[6 wt.% TiO₂] polymer electrolytes. Ionic conductivities are enhanced upon plasticization effect. Such predominant phenomenon is correlated with free volume increment.

Ionic conductivities had increased upon temperature increment (as shown in Figure 5). Such preference phenomenon is attributed to free volume increment. In general, ionic diffusional motion is enhanced upon free volume increment. In addition, local segmental relaxation is enhanced upon free volume increment. Main structural relaxation is subjected through rapid internal motion (i.e., significant rotational transition).

log σ versus 1000/T plot is almost linear in [MG49-25.0 wt.% LiClO₄]:[8.0 wt.% HNO₃-THF/TiO₂-SiO₂] polymer electrolyte. In such a case, Arrhenius behavior is predominant throughout the entire temperature range. Arrhenius behavior is described through the relation:

$$\sigma = \sigma_0 \exp \left[\frac{-E_a}{RT} \right], \quad (2)$$

where σ is conductivity (S·cm⁻¹); σ_0 is preexponential factor (S·cm⁻¹); E_a is activation energy (J·mol⁻¹); R is perfect gas constant (8.314 J·mol⁻¹·K⁻¹); and T is absolute temperature

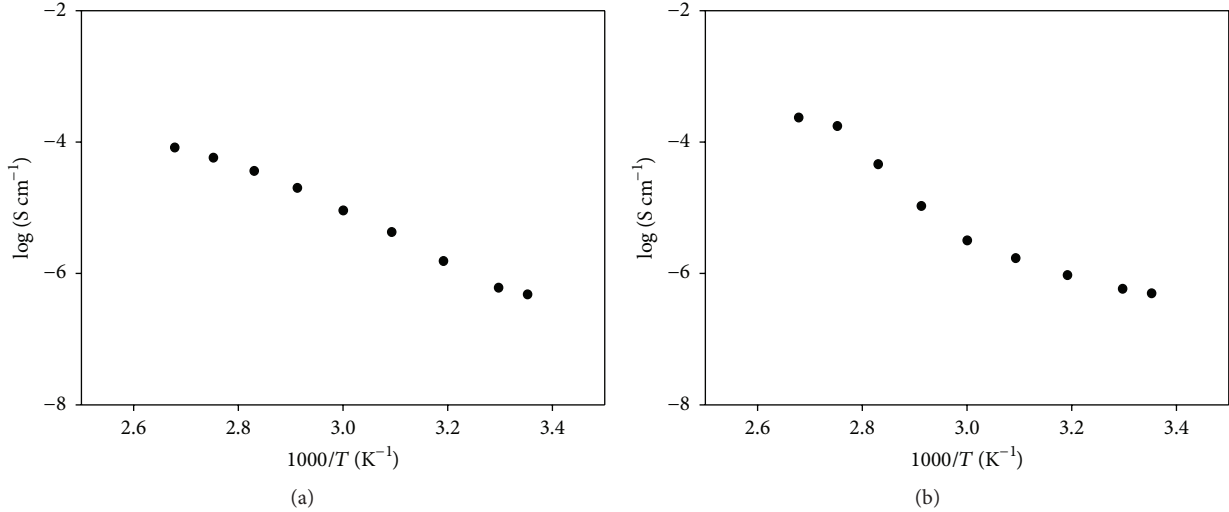


FIGURE 5: Temperature-dependence ionic conductivities: (a) [MG49-25.0 wt.% LiClO₄]:[8.0 wt.% HNO₃-THF/TiO₂-SiO₂] and (b) [MG49-25.0 wt.% LiClO₄]:[8.0 wt.% ClHNO₂-THF/TiO₂-SiO₂] polymer electrolytes.

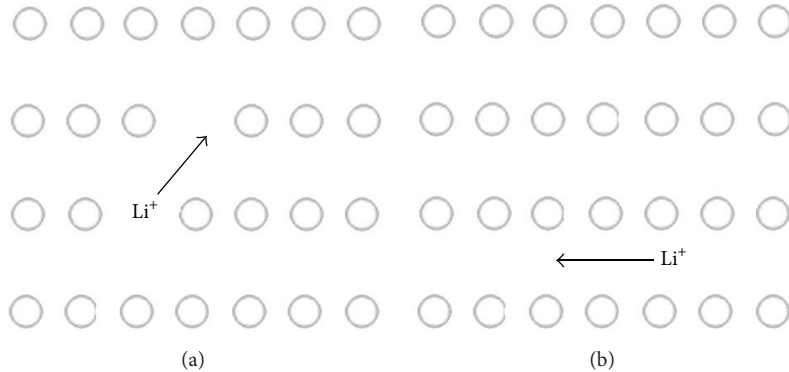


FIGURE 6: Grain lattice diffusion: (a) substitutional diffusion and (b) interstitial diffusion.

(K). In the present case, hysteresis phenomenon is not observed at high temperature range.

Ionic transport process is mediated through point defect movement. Schematic diagram is shown in Figure 6. Ionic transport process does take place in the empty sites, either vacant or interstitial sites.

$\log \sigma$ versus $1000/T$ plot is polynomial in [MG49-25.0 wt.% LiClO₄]:[8.0 wt.% ClHNO₂-THF/TiO₂-SiO₂] polymer electrolyte. In such a case, VTF behavior is revealed in the entire temperature range. VTF behavior is described through the relation:

$$\sigma = \sigma_0 \exp \left[\frac{-B}{T - T_0} \right], \quad (3)$$

where σ is ionic conductivities ($S \cdot cm^{-1}$); σ_0 is preexponential factor ($S \cdot cm^{-1}$); B is pseudo activation energy ($J \cdot mol^{-1}$); T is experimental temperature (K); and T_0 is reference temperature (K). Continuous curvature is indicative to cooperative mechanisms: segmental relaxation and/or interfacial defect interaction.

Ionic transport process is facilitated through segmental relaxation. Critical transport behavior is correlated with segmental Brownian motion. Schematic diagram is shown in Figure 7. Ionic transport process does take place in amorphous region [18].

Ionic transport process is induced through interfacial defect interaction. Critical transport behavior is correlated with interfacial site percolation [19]. Schematic diagram is shown in Figure 8. Ionic transport process does take place in space charge regions.

Distinct conductivities ($P > 0.05$) were observed in [MG49- x wt.% LiClO₄]:[8.0 wt.% HNO₃-THF/TiO₂-SiO₂] and [MG49- x wt.% LiClO₄]:[8.0 wt.% ClHNO₂-THF/TiO₂-SiO₂] polymer electrolytes. Distinct conductivities are attributed to several fundamental factors: heterophase interface structures and relative dissociation degree.

Cyclic voltammetric curves are shown in Figure 9. Pseudo-elliptic curve was observed in fast scan rate. Such feature is denoted as ideal capacitive properties. Redox peaks were not detected in the entire potential range (-0.5-0.5 Volts). Such feature is attributed to nonfaradic process.

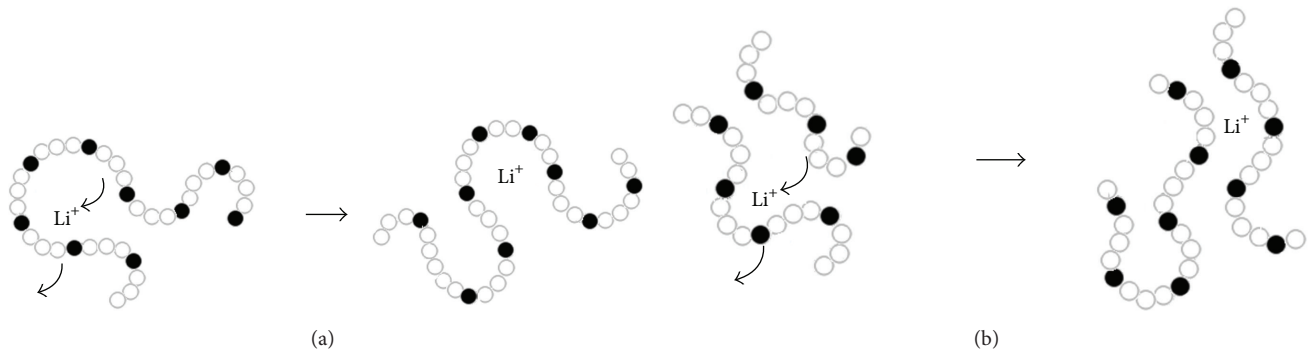


FIGURE 7: Local segmental motion: (a) intrachain motion and (b) interchain motion.

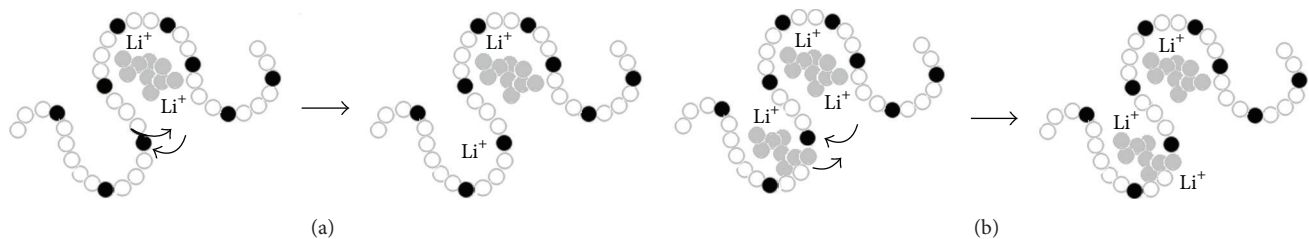


FIGURE 8: Grain boundary diffusion: (a) intrachain diffusion and (b) interchain diffusion.

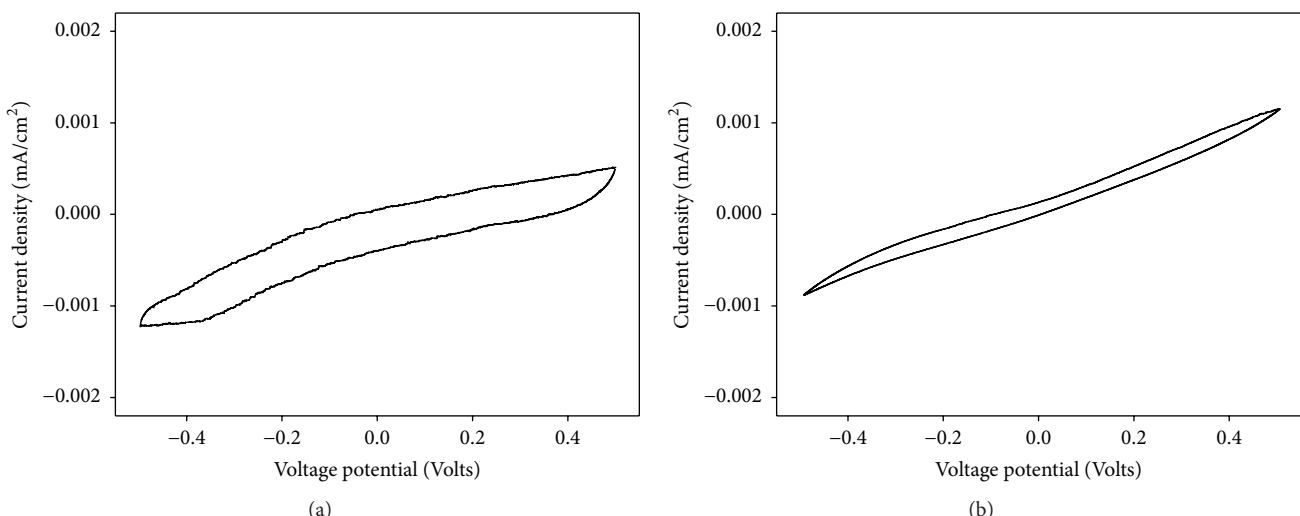


FIGURE 9: Cyclic voltammetric curves: (a) [MG49-25.0 wt.% LiClO₄]:[8.0 wt.% HNO₃-THF/TiO₂-SiO₂] and (b) [MG49-25.0 wt.% LiClO₄]:[8.0 wt.% ClHNO₃-THF/TiO₂-SiO₂] polymer electrolytes.

Broad coverage area was observed in [MG49-25.0 wt.% LiClO₄]:[8.0 wt.% HNO₃-THF/TiO₂-SiO₂] polymer electrolyte. Broad coverage area is attributed to large current efficiencies. Such preference phenomenon is associated with better capacitive behavior.

3.3. Morphological Characterization. SEM micrographs are shown in Figure 10. SEM micrographs were taken at 10,000x magnification. Uneven structure was observed throughout

entire fracture surface. Uneven structure is ascribed to polymer-salt complexation.

Irregular aggregate structure was observed throughout entire fracture surface. Irregular aggregate structure is discerned in uniform bright contrast. Irregular aggregate structure is distributed in a random fashion.

Nanoparticle dispersion state can exert influence on microstructure growth. Distinct morphological features were

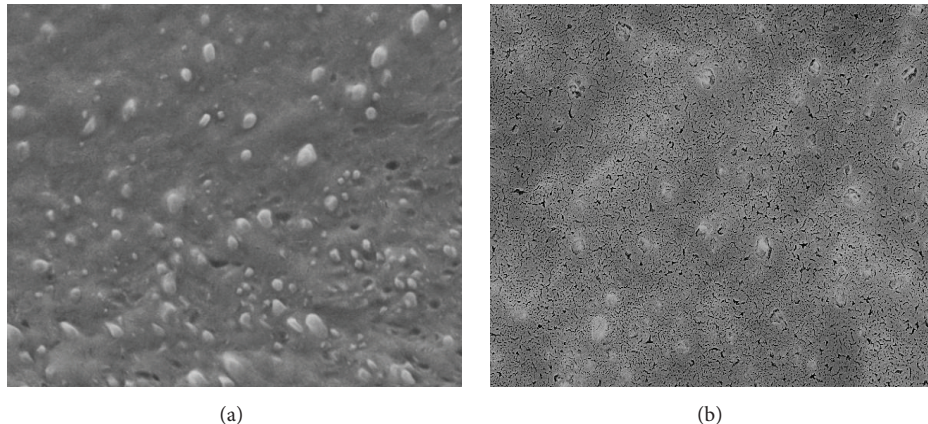


FIGURE 10: SEM micrographs: (a) [MG49-25.0 wt.% LiClO₄]:[8.0 wt.% HNO₃-THF/TiO₂-SiO₂] and (b) [MG49-25.0 wt.% LiClO₄]:[8.0 wt.% ClHNO₂-THF/TiO₂-SiO₂] polymer electrolytes.

observed in [MG49-25.0 wt.% LiClO₄]:[8.0 wt.% HNO₃-THF/TiO₂-SiO₂] and [MG49-25.0 wt.% LiClO₄]:[8.0 wt.% ClHNO₂-THF/TiO₂-SiO₂] polymer electrolytes. Continuous phase structure was observed in [MG49-25.0 wt.% LiClO₄]:[8.0 wt.% HNO₃-THF/TiO₂-SiO₂] polymer electrolyte. Continuous phase structure is attributed to crystallization retardation. Fine crack structure was observed in [MG49-25.0 wt.% LiClO₄]:[8.0 wt.% ClHNO₂-THF/TiO₂-SiO₂] polymer electrolyte. Fine crack structure is attributed to salt aggregation.

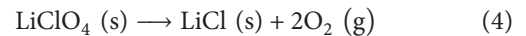
3.4. Thermal Characterization. Thermal stabilities are important parameter in performance appraisal [20]. Thermal stabilities were investigated through simultaneous thermogravimetric and differential thermal analysis.

Thermal degradation curves are shown in Figure 12. Similar degradation pattern was observed in [MG49-25.0 wt.% LiClO₄]:[8.0 wt.% HNO₃-THF/TiO₂-SiO₂] and [MG49-25.0 wt.% LiClO₄]:[8.0 wt.% ClHNO₂-THF/TiO₂-SiO₂] polymer electrolytes.

Initial degradation stage was observed around 80–100°C. Such degradation stage is ascribed to moisture (and residual solvent) elimination. Large mass loss is not detected until irreversible decomposition. In this case, however, minor mass loss was observed at lower temperature range. Such interference phenomenon is associated with TiO₂-SiO₂ catalytic effects.

Distinct degradation phases were detected at high temperature region (as shown in DTG curves). Such endothermic peaks are ascribed to thermal oxidative decomposition. First degradation step was observed around 270–290°C. Such degradation step is attributed to polymer chain decomposition. Transient degradation process is initiated through different chemical mechanisms: random-chain scission; end-chain scission; stripe formation; and cross-link formation. In the present case, thermal degradation temperature was much lower than neat MG49 decomposition (as shown in Figure 11). Such interference phenomenon is attributed to polymer-salt interaction.

Second degradation step was observed around 420–440°C. Such degradation step is attributed to LiClO₄ decomposition:



In the present case, thermal degradation temperature was much lower than pure LiClO₄ decomposition (as shown in Figure 11). Such interference phenomenon is attributed to polymer-salt interaction.

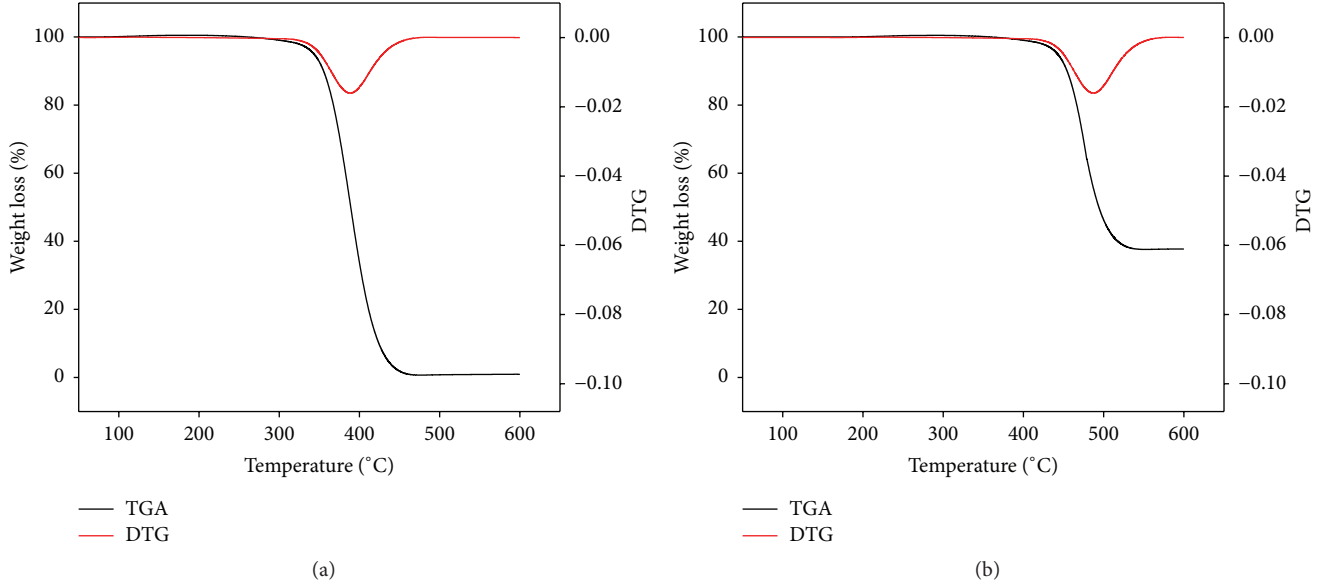
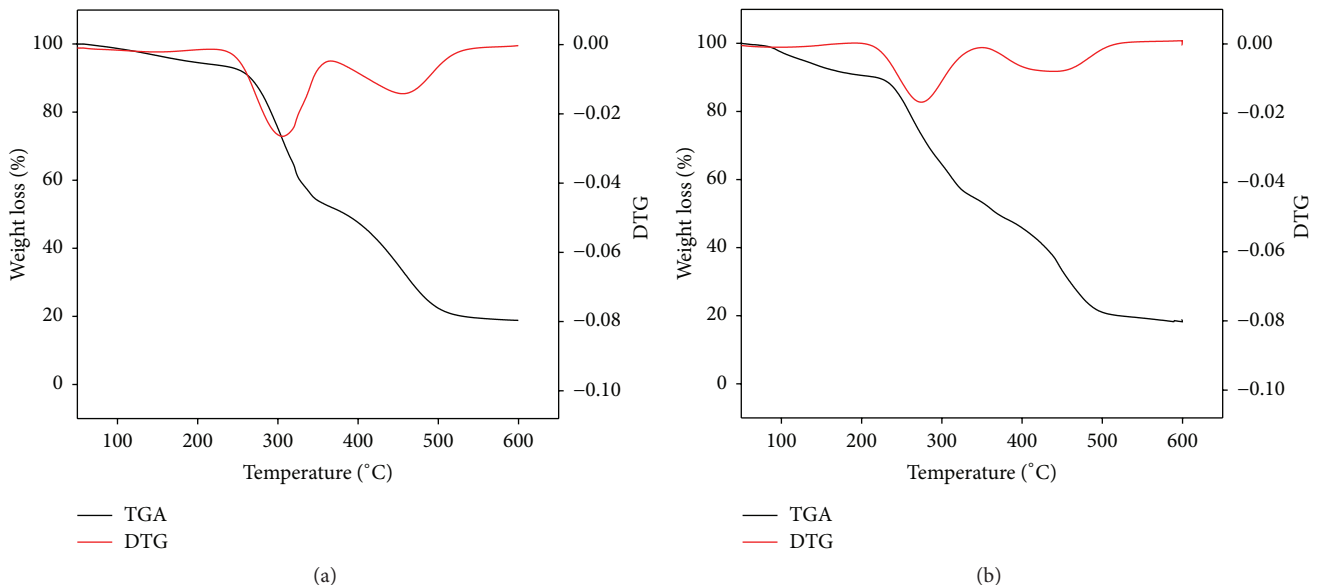
3.5. Rheological Characterization. Strain sweep tests were performed at a fixed angular frequency $\omega = 1 \text{ rad/s}$. Strain sweep profiles are shown in Figure 13.

G' and G'' moduli had remained constant over small strain change. Such predominant phenomenon is attributed to elastic energy absorption. G' and G'' moduli had sloped downward at moderate strain level. Such predominant phenomenon is attributed to network deformation. G' and G'' moduli had declined above critical strain level. Such predominant phenomenon is attributed to network breakdown (as shown in Figure 14). In general, finite chain extensibility is associated with network breakdown.

G'/G'' modulus was observed in [MG49-25.0 wt.% LiClO₄]:[8.0 wt.% HNO₃-THF/TiO₂-SiO₂] polymer electrolyte. G' modulus is dominant at low strain range. Such predominant phenomenon is attributed to high stiffness properties, that is, homogeneous reinforcement dispersion and/or significant stress transfer.

G'/G'' modulus was not observed in [MG49-25.0 wt.% LiClO₄]:[8.0 wt.% ClHNO₂-THF/TiO₂-SiO₂] polymer electrolyte. G'' modulus is dominant over the entire strain range. Such predominant phenomenon is attributed to the viscous effects.

Frequency sweep tests were performed in the linear viscoelastic range. Frequency sweep profiles are shown in Figure 15. Rectangular hyperbola curves were obtained in the linear viscoelastic region. Plateau modulus does not appear in low frequency range. Such predominant phenomenon is related to partial intercalative structure. $\log G'$ versus $\log \omega$

FIGURE 11: Thermal degradation curves: (a) neat MG49 and (b) pure LiClO_4 .FIGURE 12: Thermal degradation curves: (a) [MG49-25.0 wt.% LiClO_4]:[8.0 wt.% $\text{HNO}_3\text{-THF/TiO}_2\text{-SiO}_2$] and (b) [MG49-25.0 wt.% LiClO_4]:[8.0 wt.% $\text{ClHNO}_2\text{-THF/TiO}_2\text{-SiO}_2$] polymer electrolytes.

slope is close to 2. Such predominant phenomenon is related to heterogeneous structure.

G'/G'' modulus was observed in [MG49-25.0 wt.% LiClO_4]:[8.0 wt.% $\text{HNO}_3\text{-THF/TiO}_2\text{-SiO}_2$] and [MG49-25.0 wt.% LiClO_4]:[8.0 wt.% $\text{ClHNO}_2\text{-THF/TiO}_2\text{-SiO}_2$] polymer electrolytes. G' modulus is dominant at high frequency range. Such predominant phenomenon is attributed to rotational hindrance. In general, individual segmental relaxation is restricted upon rotational hindrance [21]. In contrast, local chain motion is not affected upon rotational hindrance. Local chain motion is governed through translational diffusion.

4. Conclusion

Different measurement techniques were further implemented in microstructural characterization. XRD analysis had revealed remarkable crystalline reduction upon structural alternation. FTIR analysis had confirmed $\text{C}=\text{O}-\text{Li}^+$ complex formation upon coordinative interaction. EIS analysis had demonstrated unique transport mechanism upon interfacial interaction. CV analysis had indicated significant redox stabilization upon interfacial interaction. TGA analysis had indicated rapid oxidative degradation upon structural

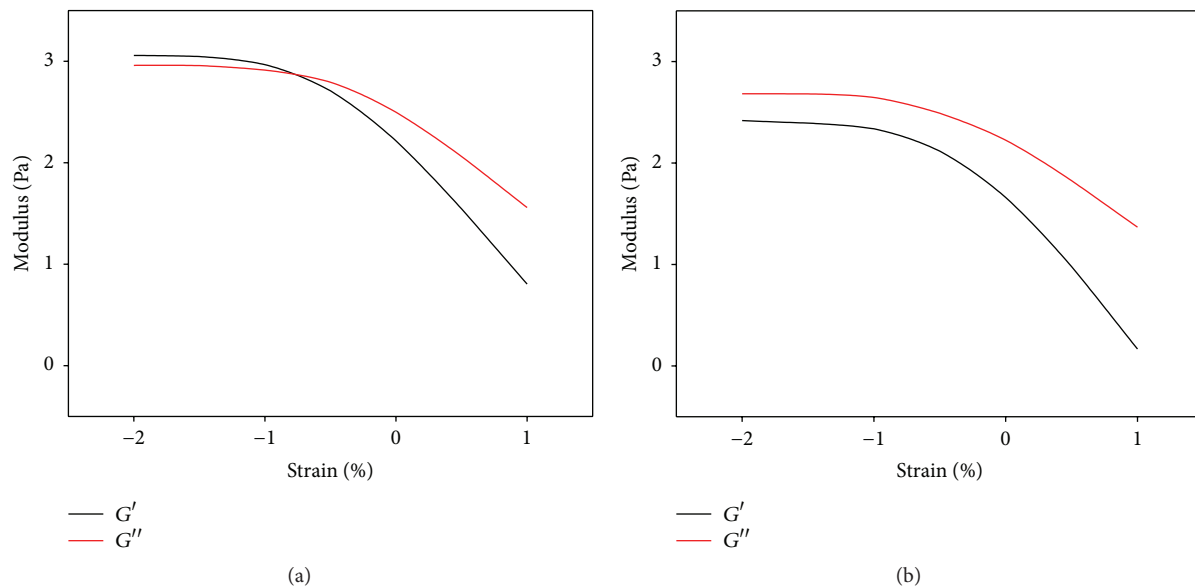


FIGURE 13: Strain sweep curves: (a) [MG49-25.0 wt.% LiClO₄]:[8.0 wt.% HNO₃-THF/TiO₂-SiO₂] and (b) [MG49-25.0 wt.% LiClO₄]:[8.0 wt.% ClHNO₂-THF/TiO₂-SiO₂] polymer electrolytes.

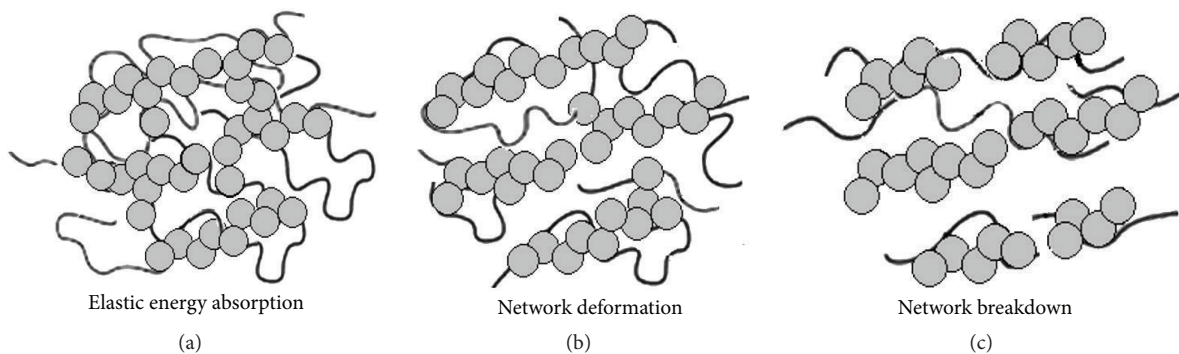


FIGURE 14: Stress-strain relations.

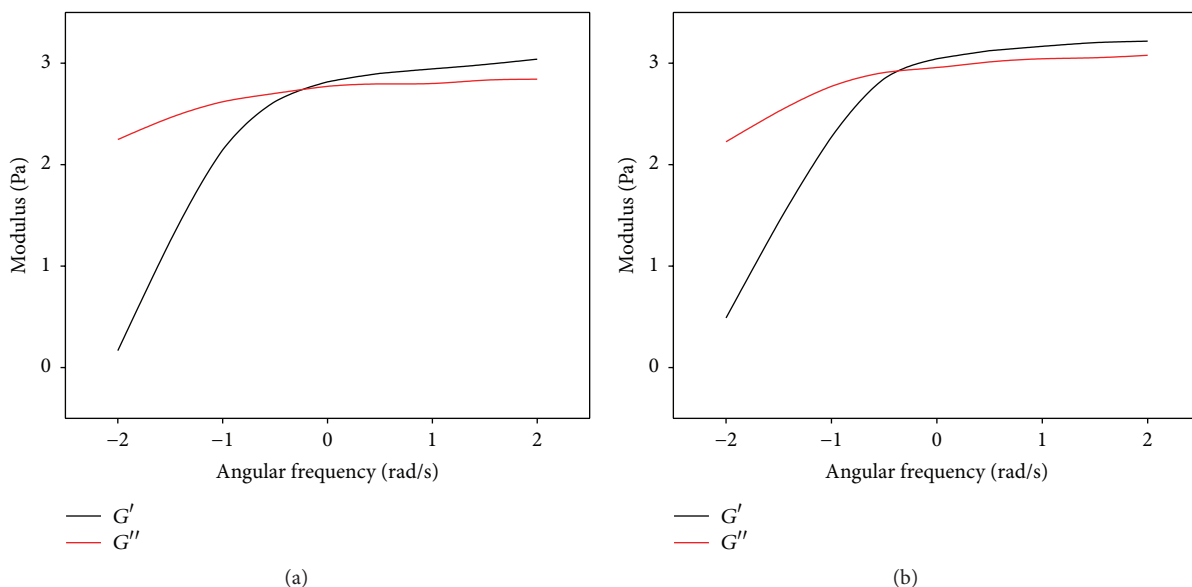


FIGURE 15: Frequency sweep curves: (a) [MG49-25.0 wt.% LiClO₄]:[8.0 wt.% HNO₃-THF/TiO₂-SiO₂] and (b) [MG49-25.0 wt.% LiClO₄]:[8.0 wt.% ClHNO₂-THF/TiO₂-SiO₂] polymer electrolytes.

alternation. DRA analysis had revealed noticeable rheological stabilization upon interparticle interaction.

Competing Interests

The authors declare that they have no competing interests.

Acknowledgments

Oon Lee Kang would like to extend his sincere appreciation to Universiti Kebangsaan Malaysia for financial support through Research Grant: NND/NM(2)/TD11-046, ERGS/1/2013/TK07/UKM/02/4, and FRGS/1/2014/ST01/UKM/02/1. Oon Lee Kang would also like to extend his sincere appreciation to the CRIM for technical support. Usman Ali Rana would like to extend his sincere appreciation to King Saud University for financial support through Prolific Research Group, Project no. PRG-1436-18.

References

- [1] C. J. Leo, G. V. Subba Rao, and B. V. R. Chowdari, "Studies on plasticized PEO-lithium triflate-ceramic filler composite electrolyte system," *Solid State Ionics*, vol. 148, no. 1-2, pp. 159–171, 2002.
- [2] G. Mao, M.-L. Saboungi, D. L. Price, Y. S. Badyal, and H. E. Fischer, "Lithium environment in PEO-LiClO₄ polymer electrolyte," *Europhysics Letters*, vol. 54, no. 3, pp. 347–353, 2001.
- [3] D. Saikia and A. Kumar, "Ionic transport in P(VDF-HFP)-PMMA-LiCF₃SO₃-(PC + DEC)-SiO₂ composite gel polymer electrolyte," *European Polymer Journal*, vol. 41, no. 3, pp. 563–568, 2005.
- [4] M. Yang and J. Hou, "Membranes in lithium ion batteries," *Membranes*, vol. 2, no. 3, pp. 367–383, 2012.
- [5] F. Croce, L. Persi, F. Ronci, and B. Scrosati, "Nanocomposite polymer electrolytes and their impact on the lithium battery technology," *Solid State Ionics*, vol. 135, no. 1–4, pp. 47–52, 2000.
- [6] M. Z. S. Fadli and A. L. Famiza, "SiO₂ filler as interface modifier in PMMA/ENR 50 electrolytes," *Advanced Materials Research*, vol. 812, pp. 120–124, 2013.
- [7] M. H. Khanmirzaei and S. Ramesh, "Nanocomposite polymer electrolyte based on rice starch/ionic liquid/TiO₂ nanoparticles for solar cell application," *Measurement*, vol. 58, pp. 68–72, 2014.
- [8] H.-W. Chen, C.-Y. Chiu, H.-D. Wu, I.-W. Shen, and F.-C. Chang, "Solid-state electrolyte nanocomposites based on poly(ethylene oxide), poly(oxypropylene) diamine, mineral clay and lithium perchlorate," *Polymer*, vol. 43, no. 18, pp. 5011–5016, 2002.
- [9] J. Zhang, H. Han, S. Wu et al., "Conductive carbon nanoparticles hybrid PEO/P(VDF-HFP)/SiO₂ nanocomposite polymer electrolyte type dye sensitized solar cells," *Solid State Ionics*, vol. 178, no. 29–30, pp. 1595–1601, 2007.
- [10] H. H. Sumathipala, J. Hassoun, S. Panero, and B. Scrosati, "High performance PEO-based polymer electrolytes and their application in rechargeable lithium polymer batteries," *Ionics*, vol. 13, no. 5, pp. 281–286, 2007.
- [11] A. S. Kamisan, T. I. T. Kudin, A. M. M. Ali, and M. Z. A. Yahya, "Polymer gel electrolytes based on 49% methyl-grafted natural rubber," *Sains Malaysiana*, vol. 40, no. 1, pp. 49–54, 2011.
- [12] G. C. Psarras, G. A. Sofos, A. Vradis et al., "HNBR and its MWCNT reinforced nanocomposites: crystalline morphology and electrical response," *European Polymer Journal*, vol. 54, no. 1, pp. 190–199, 2014.
- [13] S. H. Kim, M. J. Misner, L. Yang, O. Gang, B. M. Ocko, and T. P. Russell, "Salt complexation in block copolymer thin films," *Macromolecules*, vol. 39, no. 24, pp. 8473–8479, 2006.
- [14] S. Rajendran and T. Uma, "Conductivity studies on PVC/PMMA polymer blend electrolyte," *Materials Letters*, vol. 44, no. 3, pp. 242–247, 2000.
- [15] S. K. Deraman, N. S. Mohamed, and R. H. Y. Subban, "Ionic liquid incorporated pvc based polymer electrolytes: electrical and dielectric properties," *Sains Malaysiana*, vol. 43, no. 6, pp. 877–883, 2014.
- [16] B. Chatterjee, N. Kulshrestha, and P. Gupta, "Nano composite solid polymer electrolytes based on biodegradable polymers starch and poly vinyl alcohol," *Measurement*, vol. 82, pp. 490–499, 2016.
- [17] K. Rokesh, S. Anandan, and K. Jothivenkatachalam, "Polymer electrolytes in dye sensitized solar cells," *Materials Focus*, vol. 4, no. 4, pp. 262–271, 2015.
- [18] S. Rajendran, T. Mahalingam, and R. Kannan, "Experimental investigations on PAN-PEO hybrid polymer electrolytes," *Solid State Ionics*, vol. 130, no. 1, pp. 143–148, 2000.
- [19] W. Dieterich, O. Dürr, P. Pendzig, A. Bunde, and A. Nitzan, "Percolation concepts in solid state ionics," *Physica A: Statistical Mechanics and Its Applications*, vol. 266, no. 1–4, pp. 229–237, 1999.
- [20] K.-S. Kim, S.-Y. Park, S.-H. Yeon, and H. Lee, "N-Butyl-N-methylmorpholinium bis(trifluoromethanesulfonyl)imide-PVdF(HFP) gel electrolytes," *Electrochimica Acta*, vol. 50, no. 28, pp. 5673–5678, 2005.
- [21] J. Kalfus, N. Singh, and A. J. Lesser, "Reinforcement in nano-filled PAA hydrogels," *Polymer*, vol. 53, no. 13, pp. 2544–2547, 2012.



Journal of
Nanotechnology



International Journal of
Corrosion



International Journal of
Polymer Science



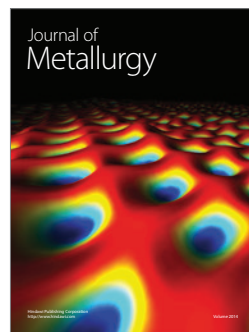
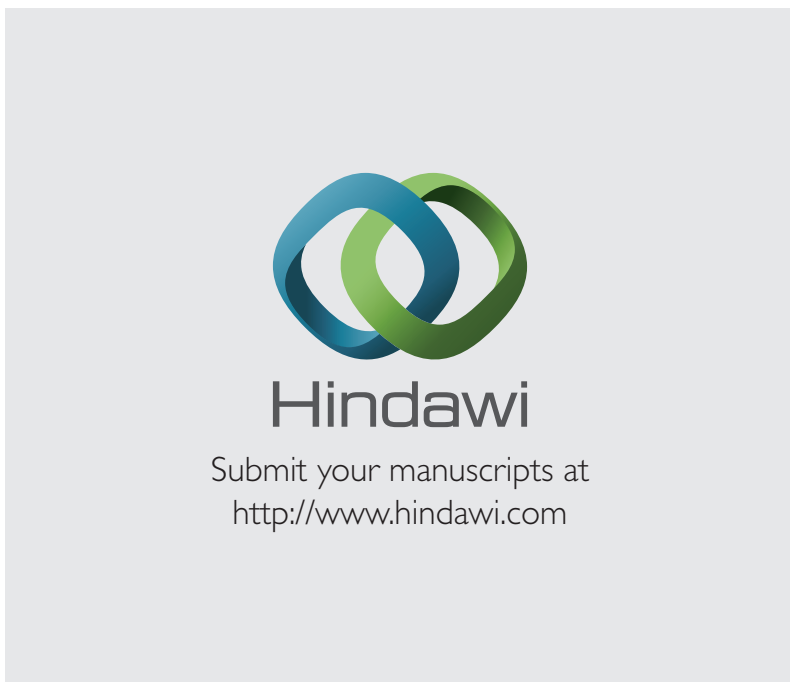
Smart Materials
Research



Journal of
Composites



BioMed
Research International



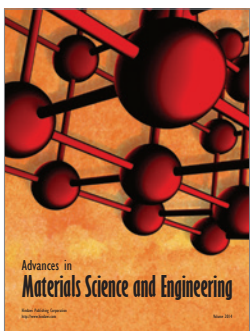
Journal of
Metallurgy



Journal of
Materials



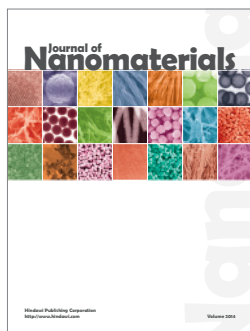
Journal of
Nanoparticles



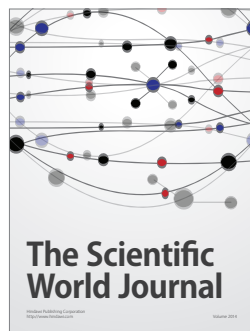
Advances in
Materials Science and Engineering



Scientifica



Journal of
Nanomaterials



The Scientific
World Journal



International Journal of
Biomaterials



Journal of
Nanoscience



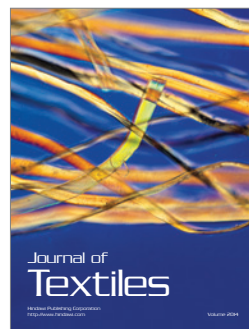
Journal of
Coatings



Journal of
Crystallography



Journal of
Ceramics



Journal of
Textiles